A Special Shell Element Formulation and Implementation for Reliable Fatigue Evaluation of Spot-Welded Structures

Lunyu Zhang, Shengjia Wu and Pingsha Dong[1]
Naval Architecture and Marine Engineering
University of Michigan
Ann Arbor, MI 48109, USA

March 2, 2024

Abstract

As virtual engineering becomes increasingly important in today's competitive marketplace, there is a growing need for simplified representations of spot joints in finite element (FE) modeling of complex structures without sacrificing accuracy in structural life evaluation. For this purpose, this paper presents a special shell element with an implicit spot weld representation and its numerical implantation as a user element for deployment in commercial FE code for reliably computing traction structural stress in a mesh-insensitive manner. The special shell element is formulated by degenerating conventional linear four-nodes Mindlin shell elements with consideration of the region around a spot weld by imposing kinematic constraints with respect to a series of virtual nodes. The simplicity and effectiveness of the special shell element have been validated by comparing with the explicit weld representation for computing mesh-insensitive structural stresses and fatigue life correlation of welded components.

Keywords: user-element; shell element, spot weld element; structural stress; mesh-insensitivity; spot weld; spot joint; fatigue evaluation

[1] Corresponding author. Tel.:+1-734-615-7484

Email address: dongp@umich.edu (Pingsha Dong)

1. Introduction

Typical automotive structures like passenger cars and commercial vehicle cabs contain about 3,000 and 7,000 spot welds, respectively, as discussed in [1, 2, 3]. Resistance spot welding (RSW), and more recently laser or friction stir spot welding, serves as a cost-effective means for joining metal sheets together to form lightweight load-bearing structures, as recently discussed in Bhatti et al. [1], Junqueira et al. [2], and Yan et al. [3]. Other joining methods like self-piercing rivets (SPR) [4], rivet-welded (RW) joints [5] and etc., as described in [6] are also increasingly used for assembly of dissimilar materials for advanced lightweight automotive structures [7]. It should be noted that fatigue behaviors in these joint types share similar characteristics, as far as major failure modes are concerned [8]. These failure modes can be classified as Mode A: sheet failure around the joint and Mode B: weld nugget failure (or rivet failure in rivetted joints), as shown in Figure 1. Mode A is most important for structural fatigue evaluation since Mode B can be effectively avoided by specifying an adequate spot weld size or rivet size, as discussed in [8] and [9].

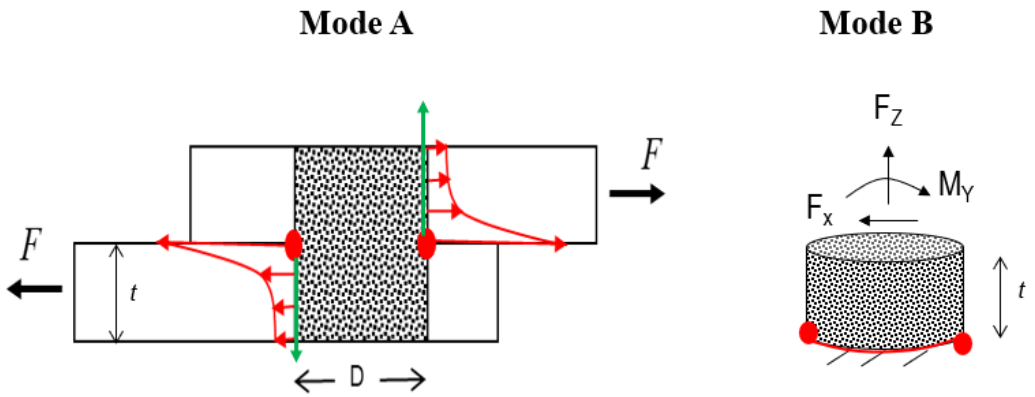

Figure 1. The schematic of two failure modes. Mode A (left): fatigue cracking from the interfacial notch into the sheet. Mode B (right): fatigue cracking from the interfacial notch into the weld nugget.

For properly evaluating Mode A failure mode in spot-welded structures, a finite element model (FEM) needs to have an explicit and complete representation of a weld periphery on the connected sheets, e.g., along the spot weld nugget edge in the base plate, as shown in Figure 2 [10]. In typical automotive structures containing thousands of spot welds, such a spot weld representation procedure, has been impractical. Note that simplified methods available to date, e.g., FE representation schemes using ACM2 or CWELD [11] with the stress parameters calculated via Rupp's LBF method [8], have been shown inadequate and therefore, require costly calibrations through fatigue testing and past experiences. As virtual engineering becomes increasingly important, auto makers and their suppliers strive to remain competitive in the global marketplace by minimizing or eliminating hardware testing in their vehicle development processes. This has become particularly challenging as automotive structures are going through a major paradigm shift towards battery electric vehicles (BEV) for which there exist no prior experiences nor sufficient historical test data upon which existing structural durability evaluation tools can be calibrated.

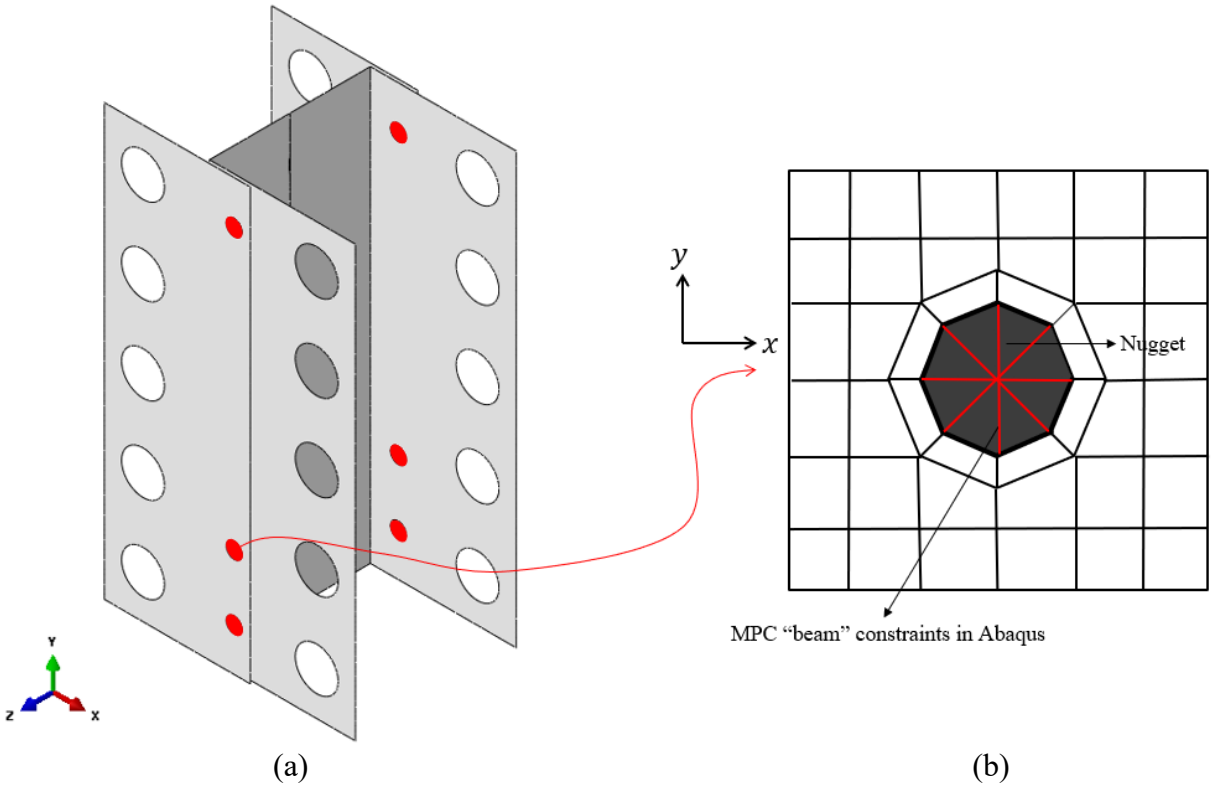

Figure 2. The schematic of a spot-welded H-Shear component [10] and required weld representation in a finite element model: (a) illustration of a spot welded H-shear component; (b) an explicit finite element representation of spot weld joining the steel sheets.

Therefore, a simple and effective spot joint modeling method is highly desirable. Along this line, Zhang et al. [12] recently presented a hybrid method which is capable of producing reasonable structural stress results through a novel decomposition technique by taking advantage of a set of analytical solutions available in the literature. With this technique, the nodal forces and moments obtained around a group of shell elements surrounding the weld nugget, as shown in Figure 3, are decomposed into a series of simple load cases for which analytical structural stress solutions based on shell theory are already available [13, 14, 15]. The final structural stress solutions can then be obtained through superposition. While the coarse-mesh hybrid structural stress method in Zhang et al. [12] was shown producing reasonably accurate for structural stress results for simple laboratory test specimens, its applications for modeling

complex spot-welded structures are still limited by both the lack of closed-form solutions in literature for some of the load cases that must be considered when dealing with complex loading conditions [12-14,16] and the inability of coarse elements for representing complex sheet deformation mode around a weld nugget.

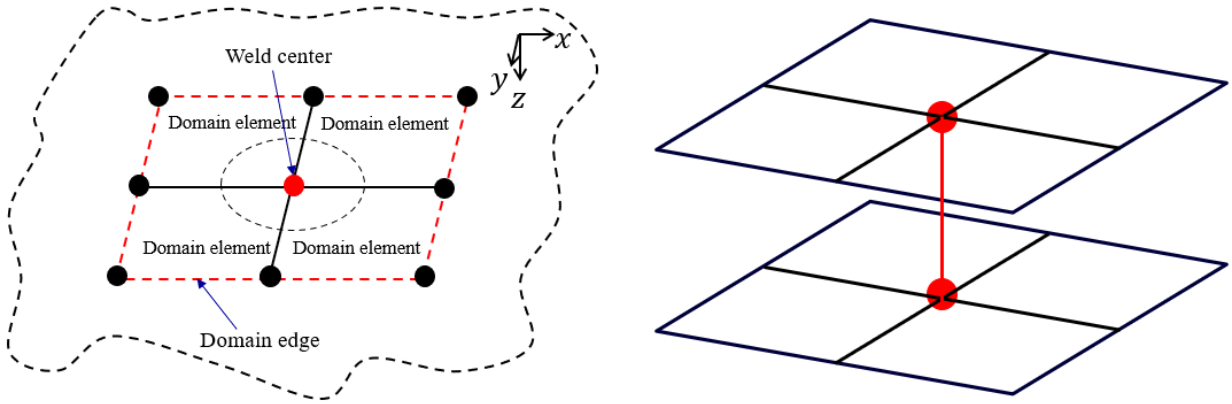

Figure 3. Illustration of the coarse mesh hybrid structural stress modeling method in Zhang et.al [12]: (a) a rectangular spot weld region in a component; (b) a simplified finite element representation of the spot weld region.

To address the above deficiencies associated with the coarse-mesh hybrid structural stress method in Zhang et al. [12], a special shell element incorporating spot weld deformation constraints is presented in this paper, hereafter referred to as Spot Weld Element (SWE). In Section 2, we start with the SWE formulation by considering two linear four-node Mindlin shell elements embedded with a series of virtual nodes representing a curved weld edge position which must satisfy the kinematic constraints and equilibrium conditions consistent with those if an actual weld is present. The numerical implementation of SWE in the form of user element (often referred to as "UEL") in commercial FE codes, e.g., ABAQUS, is then described, along with how the nodal forces and moments along the virtual weld edge represented by virtual nodes are used for computing the mesh-insensitive structural stress distribution. Validations are presented in Section 3. These include detailed comparisons of computational results on single

spot-welded lab specimens and spot-welded complex components among various methods. The effectiveness of the SWE proposed for correlating fatigue test data collected from two types of "H-Section" components, i.e., H-shear and H-peel [10], is given in Section 4. Key findings are given in Section 5.

2. Spot Weld Element (SWE) Formulation

2.1 Structural stress definition

Figure 4(a) shows a through-thickness curvilinear cut plane into sheet thickness around a spot weld edge on which there exist three traction-based structural stress components under general loading conditions. The three structural stress components, i.e., the normal, in-plane shear, and transverse shear structural stresses, can be directly expressed in terms of the equilibrium-equivalent line forces (f_r, f_θ, f_z) and line moments (m_r, m_θ) computed through the nodal forces and nodal moments obtained from FEA along the spot weld edge. Note that the nodal forces and moments are defined with respect to a global fixed coordinate system (X, Y, Z) while line forces and moments are defined with respect to the local coordinate system (r, θ, z) at the weld center shown in Figure 4(b). The line forces (f_r, f_θ, f_z) and line moments (m_r, m_θ) can be solved using a system of simultaneous equations as described in [17, 18] which will be further discussed in a latter section. Finally, the traction-based structural stress components can be expressed as follows:

$$\begin{aligned} \sigma_s &= \sigma_m + \sigma_b = \frac{f_r}{t} - \frac{6m_\theta}{t^2} \\ \tau_s &= \tau_m + \tau_b = \frac{f_\theta}{t} + \frac{6m_r}{t^2} \\ \tau_z &= \frac{f_z}{t} \end{aligned} \tag{1}$$

where σ_s is normal stress, τ_s is in-plane shear stress, τ_z is transverse shear stress, and t is plate thickness. In general, the normal stress σ_s and in-plane shear stress τ_s are expressed in terms of their membrane and bending components, i.e., membrane stress σ_m and bending stress σ_b for normal stress σ_s and membrane stress τ_m and bending stress τ_b for in-plane shear stress τ_s. Note that the transverse shear stress τ_z is represented only by membrane part of the transverse shear force in Equation (1).

It should be emphasized that the computational procedure for the three traction-based structural stress components are given in Dong et al. [19] by using the nodal forces and moments from shell elements along the nodal positions representing the spot weld edge as shown in Figure 4(c) for achieving element size insensitivity.

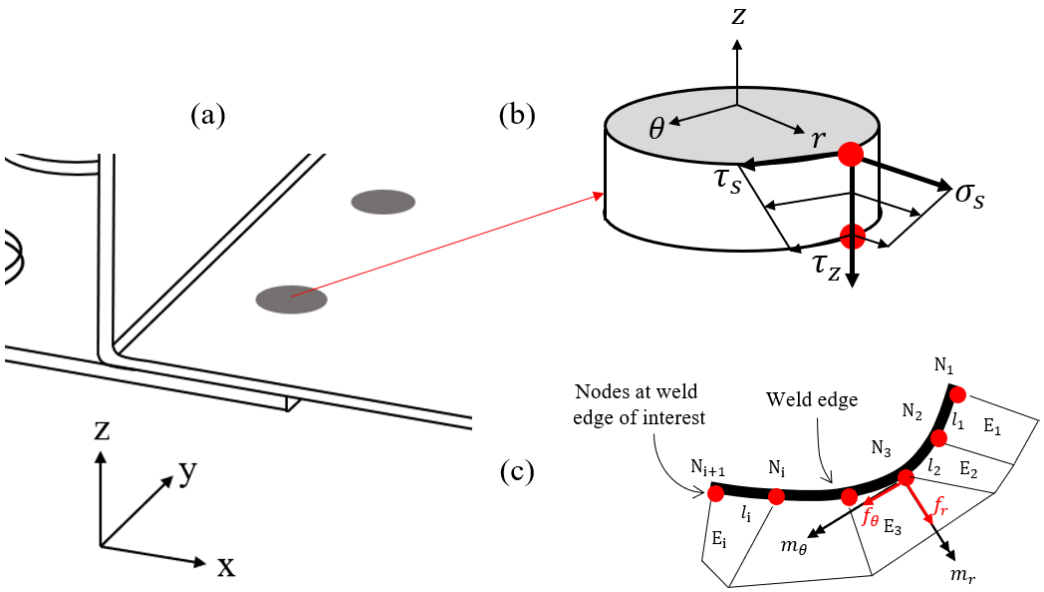

Figure 4. Illustration of structural stresses in welded components: (a) the close-up view near a spot weld in the modified H-shear component [10];(b) the definition of three traction-based structural stress components near weld edge; (c) the nodes and elements at weld edge in FEM for evaluation of structural stresses.

2.2 Spot Weld Element (SWE)

Without losing generality, we consider the same representative spot weld region as illustrated in Figure 3(b). Due to the presence of the spot weld, its local stiffness with respect to relevant degrees of freedom can be assumed as being equivalent to a rigid inclusion [20], as originally introduced by Radaj and Zhang [21] for modeling simple spot-welded test specimens. As such, the concept of SWE is described in Figure 5 in which two conventional linear Mindlin shell elements neighboring a sector of a rigid inclusion are used to represent a quarter of the square domain in Figure 3. As shown in Figure 5(a), the 1st shell element consists of 4 nodes with the numbering sequence as v1-2-3-v2 and the 2nd shell element consists of 4 nodes with the numbering sequence as v2-3-4-v3. Nodes v1, v2, and v3 represent the rigid inclusion (spot weld) boundary of radius a measured from its center defined by Node 1. Therefore, Nodes 1, v1, v2, and v3 form a quarter of a circular inclusion region. Within the inclusion or spot weld region, its effects on the two neighboring shell elements can be described through a set of kinematic constraints and force/moment equilibrium conditions, leading to the formulation of its equivalent four-node special shell element shown in Figure 5(b) by following steps which will be explained in details in latter sections:

1st Step: The element stiffnesses for Element #1 and Element #2 are derived.

2nd Step: The kinematic constraints and force/moment equilibrium conditions are applied at Node pairs 1-v1, 1-v2, and 1-v3.

3rd Step: The stiffness matrix corresponding to the SWE shown in Figure 5(b) is assembled.

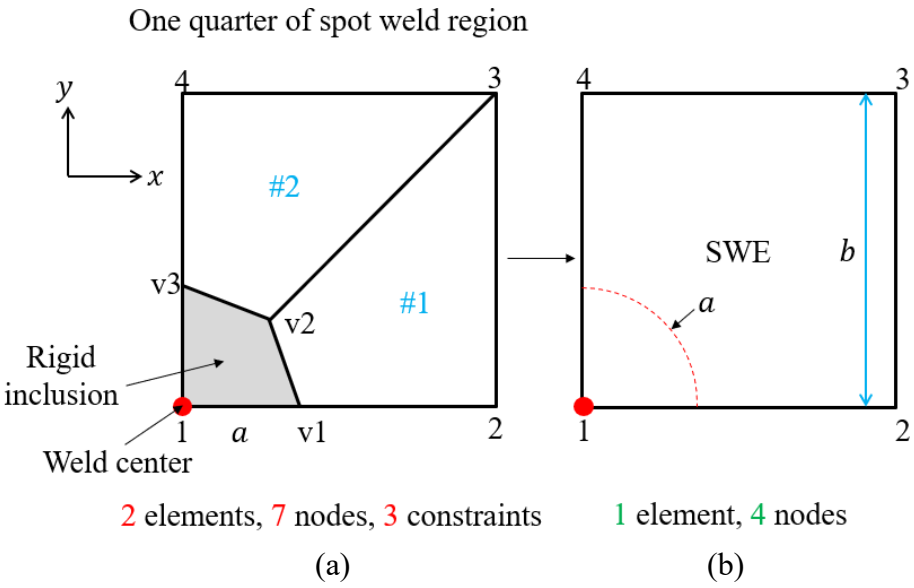

Figure 5. Illustration of SWE: (a) a schematic of the explicit and complete FEM of one quarter of spot weld region; (b) the SWE of one quarter of spot weld region.

2.3 Kinematic and Equilibrium Conditions around Spot Weld

By considering the spot weld as a rigid inclusion in Figure 5(a), the following kinematic constraints needs to be satisfied with respect to the coordinate system defined in Figure 5:

$$
\begin{aligned}
u^i &= u^1 - \theta_z^1 \times \left(y^i - y^1\right) \\
v^i &= v^1 + \theta_z^1 \times \left(x^i - x^1\right) \\
w^i &= w^1 + \theta_x^1 \times \left(y^i - y^1\right) - \theta_y^1 \times \left(x^i - x^1\right) \\
\theta_x^i &= \theta_x^1 \\
\theta_y^i &= \theta_y^1 \\
\theta_z^i &= \theta_z^1
\end{aligned}
\tag{2}
$$

where u^i, v^i, w^i, are the translational displacements, θ_x^i, θ_y^i, θ_z^i are the rotations at virtual node i, with i = v1, v2, and v3, and u^1, v^1, w^1, θ_x^1, θ_y^1, θ_z^1 are the corresponding displacements and rotations at Node 1. The $x^i - x^1$ and $y^i - y^1$ are differences of local coordinates or local distances between virtual Nodes v1, v2, v3 and 1. Due to the kinematic constraints in Equation

(2), only the displacements and rotations at Node 1 are independent degrees of freedom (DOFs). The displacements and rotations at virtual nodes v1, v2, and v3 are dependent DOFs.

The nodal positions defining the inclusion boundary , e.g., Nodes 1, v1, v2, and v3, must satisfy the force and moment equilibrium conditions:

$$
\begin{aligned}
F_x^1 &= \sum_{i=v1}^{v3} F_x^i \\
F_y^1 &= \sum_{i=v1}^{v3} F_y^i \\
F_z^1 &= \sum_{i=v1}^{v3} F_z^i \\
M_x^1 &= \sum_{i=v1}^{v3} M_x^i + \sum_{i=v1}^{v3} F_z^i \times \left(y^i - y^1 \right) \\
M_y^1 &= \sum_{i=v1}^{v3} M_y^i - \sum_{i=v1}^{v3} F_z^i \times \left(x^i - x^1 \right) \\
M_z^1 &= \sum_{i=v1}^{v3} M_z^i - \sum_{i=v1}^{v3} F_x^i \times \left(y^i - y^1 \right) + \sum_{i=v1}^{v3} F_y^i \times \left(x^i - x^1 \right)
\end{aligned}
\tag{3}
$$

where F_x^i, F_y^i, F_z^i are the forces act at virtual nodes v1, v2, v3, M_x^i, M_y^i, M_z^i are the moments act at virtual nodes v1, v2, v3, and F_x^1, F_y^1, F_z^1 are the forces and M_x^1, M_y^1, M_z^1 are the moments act at Node 1. From Equation (3), the nodal forces and nodal moments at virtual nodes can be transferred to Node 1.

2.4 SWE Element Stiffness Assembly

For convenience, we first define the stiffness matrices of Element #1 and Element #2 in Figure 5(a) are represented as K^1 and K^2, respectively, in the following form:

$$K^i = \begin{bmatrix} k^i_{1,1} & k^i_{1,2} & \cdots & k^i_{1,23} & k^i_{1,24} \\ k^i_{2,1} & k^i_{2,2} & \cdots & k^i_{2,23} & k^i_{2,24} \\ \vdots & \vdots & k^i_{m,n} & \vdots & \vdots \\ k^i_{23,1} & k^i_{23,2} & \cdots & k^i_{23,23} & k^i_{23,24} \\ k^i_{24,1} & k^i_{24,2} & \cdots & k^i_{24,23} & k^i_{24,24} \end{bmatrix}_{24\times 24} \tag{4}$$

where i is 1 or 2 for Element #1 and Element #2, respectively. In Equation (4), $k^i_{m,n}$ represents the entry at mth row and nth column. It should be noted that the element stiffness matrices K^1 and K^2 can be easily calculated as their formulations are well documented and can be found in FEM textbooks [22].

Then, a unit displacement vector U containing displacement field at Nodes 1, 2, 3, and 4 can be defined as:

$$U = \begin{bmatrix} 1 & 0 & ... & 0 & 0 \end{bmatrix}^T_{24\times 1} \tag{5}$$

The above represents a unit displacement applied at Node 1 along X direction and other DOFs are set to zeros. Next, this unit displacement vector U is substituted into Equation (2) to generate two displacement vectors U^1 and U^2 corresponding to the displacement fields for Element #1 and Element #2, respectively:

$$\begin{aligned} U^1 &= \begin{bmatrix} 1 & 0 & 0 & 0 & 0 & 0 & 0 & 0 & 0 & 0 & 0 & 0 & 0 & 0 & 0 & 0 & 0 & 0 & 1 & 0 & 0 & 0 & 0 & 0 \end{bmatrix}^T_{24\times 1} \\ U^2 &= \begin{bmatrix} 1 & 0 & 0 & 0 & 0 & 0 & 0 & 0 & 0 & 0 & 0 & 0 & 0 & 0 & 0 & 0 & 0 & 0 & 1 & 0 & 0 & 0 & 0 & 0 \end{bmatrix}^T_{24\times 1} \end{aligned} \tag{6}$$

Then, with the element stiffness matrices K^1 of Element #1 and K^2 of Element #2, the nodal forces for Element #1 and Element #2 can be calculated as

$$\begin{aligned} K^1U^1 &= F^1 \\ K^2U^2 &= F^2 \end{aligned} \tag{7}$$

and the F^1 and F^2 are expressed as

$$
\begin{aligned}
F^1 &= \begin{bmatrix} k^1_{1,1} & k^1_{2,1} & k^1_{3,1} & k^1_{4,1} & \cdots & k^1_{21,1} & k^1_{22,1} & k^1_{23,1} & k^1_{24,1} \end{bmatrix}^T_{24\times 1} \\
F^2 &= \begin{bmatrix} k^2_{1,1} & k^2_{2,1} & k^2_{3,1} & k^2_{4,1} & \cdots & k^2_{21,1} & k^2_{22,1} & k^2_{23,1} & k^2_{24,1} \end{bmatrix}^T_{24\times 1}
\end{aligned} \tag{8}
$$

It should be mentioned again the $k^i_{m,n}$ in Equation (8) are now fully defined with the entries of element stiffness matrices being given by Equation (4).

These nodal force vectors F^1 and F^2 are then substituted into Equation (3) to generate the nodal force vector F corresponding to SWE with nodes 1, 2, 3 and 4:

$$
\begin{aligned}
F_1 &= F^1_x = k^1_{1,1} + k^1_{19,1} + k^2_{1,1} + k^2_{19,1} \\
F_2 &= F^1_y = k^1_{2,1} + k^1_{20,1} + k^2_{2,1} + k^2_{20,1} \\
F_3 &= F^1_z = k^1_{3,1} + k^1_{21,1} + k^2_{3,1} + k^2_{21,1} \\
F_4 &= M^1_x = k^1_{4,1} + k^1_{22,1} + k^2_{4,1} + k^2_{22,1} \\
&\quad + k^1_{3,1}\times\left(y^{v1} - y^1\right) + k^1_{21,1}\times\left(y^{v2} - y^1\right) + k^2_{3,1}\times\left(y^{v2} - y^1\right) + k^2_{21,1}\times\left(y^{v3} - y^1\right) \\
F_5 &= M^1_y = k^1_{5,1} + k^1_{23,1} + k^2_{5,1} + k^2_{23,1} \\
&\quad - k^1_{3,1}\times\left(x^{v1} - x^1\right) - k^1_{21,1}\times\left(x^{v2} - x^1\right) - k^2_{3,1}\times\left(x^{v2} - x^1\right) - k^2_{21,1}\times\left(x^{v3} - x^1\right) \\
F_6 &= M^1_z = k^1_{6,1} + k^1_{24,1} + k^2_{6,1} + k^2_{24,1} \\
&\quad - k^1_{1,1}\times\left(y^{v1} - y^1\right) - k^1_{19,1}\times\left(y^{v2} - y^1\right) - k^2_{1,1}\times\left(y^{v2} - y^1\right) - k^2_{19,1}\times\left(y^{v3} - y^1\right) \\
&\quad + k^1_{2,1}\times\left(x^{v1} - x^1\right) + k^1_{20,1}\times\left(x^{v2} - x^1\right) + k^2_{2,1}\times\left(x^{v2} - x^1\right) + k^2_{20,1}\times\left(x^{v3} - x^1\right) \\
F_7 &= \cdots \\
&\cdots
\end{aligned} \tag{9}
$$

Equation (9) lists the first 6 entries in the nodal force vector F. These 6 given entries are the forces and moments act at Node 1.

Finally, because the element stiffness matrix K of the SWE should satisfy:

$$KU = F \tag{10}$$

where U is given in Equation (4) and F is given in Equation (9). Because U is a unit vector, Equation (10) can be written as

$$KU = \begin{bmatrix} k_{1,1} & k_{2,1} & k_{3,1} & k_{4,1} & \cdots & k_{21,1} & k_{22,1} & k_{23,1} & k_{24,1} \end{bmatrix}^T_{24\times 1} = F \tag{11}$$

Therefore, by comparing Equation (11) and Equation (9), one can easily determine the 1st column of K.

By repeating the Equations (5) to (12) with different nonzero entry for the unit displacement vector U in Equation (5), one can calculate the entire K of the SWE. For example, by letting ith entry of U equals to 1 and the other entries equal to 0 as

$$\begin{aligned} U &= \begin{bmatrix} 0 & 0 & \cdots & 1 & \cdots & 0 & 0 \end{bmatrix}^T_{24\times 1} \\ U\left(j=i\right) &= 1 \\ U\left(j\neq i\right) &= 0 \end{aligned} \tag{12}$$

Readers can then follow the Equations (6) to (12) to calculate the ith column of K which will not be elaborated here.

It is worth noted that the entire element stiffness matrix K of the SWE has the dimensions of 24 by 24 (4 nodes with 6 DOFs per node). However, due to symmetry, only 300 entries of K are unique. In addition, because the membrane part and plate part of shell element are decoupled, only 124 entries among that 300 unique entries are nonzero.

If the SWE element by Nodes 1, 2, 3 and 4 happens to form a square with the spot weld nugget radius a, element size b, material Young's modulus E, material Poisson's ratio v, and plate thickness t, then the entry $k_{1,1}$ of element stiffness matrix K of the SWE can be expressed as:

$$k_{1,1} = \frac{1.3\times 10^{-3} Et\left(v-3\right)\left(7.7a^4 - 18.5a^3b + a^2b^2 + 25.6ab^3 - 16b^4\right)}{\left(1-v^2\right)} \tag{13}$$

Part of the stiffness matrix entries of K for the example SWE given in Figure 5(b) are documented in Appendix A for readers' reference.

It should be noted that for both parabolic elements and arbitrary-shaped quadrilateral linear elements, the combined stiffness matrix must be defined numerically by imposing Equations (2) and (3), as presented in Appendix B.

2.5 Structural Stress Computations

For comparison purpose, we first consider the conventional shell element modeling procedure for the spot weld specimen with an explicit weld representation shown in Figure 2, hereafter referred to as the reference model. In such a model, plane-remaining-plane within the weld nugget area is required, which can be implemented as "MPC beam" constraints in Abaqus [23]. Then, nodal forces and moments along weld nugget periphery (see Figure 4) are collected by completing FE analysis under given loading and boundary conditions. These nodal forces and moments are then converted to line forces and moments through Equation (14). The resulting structural stresses can then be calculated through Equation (1) [18].

In contrast, the newly formulated SWEs in Section 2.4 above offers a much simpler mesh layout around the spot weld region, as illustrated in Figure 3 in which each of the elements is a SWE element (see Figure 5b) with spot weld radius represented by a set of virtual nodes (3 in all examples reported in this paper. A total of four SWEs are used around the spot weld on the top sheet and bottom sheet, respectively. The top and bottom sheet can be simply connected by one beam element of diameter a. As such, SWEs interfaced with any commercial finite element code offer user-element interface with nodal forces and moments at the virtual nodes positioned at the spot weld periphery. Then, the existing simultaneous equations (Equation (14)), relating nodal forces/moments to line forces/moments, can be used directly for computing the structural stresses, as described below.

The mesh-insensitive structural stress methods [17, 18, 19] were developed based on the work equivalent argument that the work done by the nodal forces/moments is equal to the work done by the distributed line forces/moments, the nodal forces and moments are then converted to the line forces and moments around the nugget edge line (at virtual nodes v1, v2, v3, …). This is done through a system of simultaneous equations from [17, 18, 19] for converting nodal forces to nodal line forces along the weld nugget edge line (at virtual nodes v1, v2, v3, …), as:

$$\begin{Bmatrix} F_1 \\ F_2 \\ F_3 \\ . \\ . \\ F_{n-1} \end{Bmatrix} = \begin{bmatrix} \frac{(l_1+l_{n-1})}{3} & \frac{l_1}{6} & 0 & 0 & .. & \frac{l_{n-1}}{6} \\ \frac{l_1}{6} & \frac{(l_1+l_2)}{3} & \frac{l_2}{6} & 0 & .. & .. \\ 0 & \frac{l_2}{6} & \frac{(l_2+l_3)}{3} & \frac{l_3}{6} & .. & .. \\ .. & .. & .. & .. & .. & .. \\ .. & .. & .. & .. & .. & .. \\ \frac{l_{n-1}}{6} & 0 & 0 & 0 & \frac{l_{n-2}}{6} & \frac{(l_{n-2}+l_{n-1})}{3} \end{bmatrix} \begin{Bmatrix} f_1 \\ f_2 \\ f_3 \\ . \\ . \\ f_{n-1} \end{Bmatrix} \quad (14)$$

where f_1, f_2, f_3, ... are the local line forces at virtual nodes v1, v2, v3, ..., F_1, F_2, F_3, ... are local nodal forces in local coordinate systems at the virtual nodes v1, v2, v3, ..., and l_1, l_2, l_3, ... are the element lengths between corresponding nodes. Since the weld nugget edge line along the nugget periphery is closed, the local line force at virtual node vN is the same as the local line force at virtual node v1. Similarly, the local line moments can be calculated using the local nodal moments using the same simultaneous equations, Equation (14). With the calculated local line forces and line moments, structural stress is then calculated at each virtual nodes on the periphery of the nugget by the means of Equation (1).

3. Validation Examples

In addition to a series of one element numerical tests for a quarter of weld region provided in Appendix B, actual fatigue specimens including both simple laboratory specimens with single weld and complex multi-weld structural components are presented here to examine both the accuracy and the robustness of the SWE method for fatigue evaluation purpose.

3.1 Laboratory Specimens with Single Weld

3.1.1 Lap-Shear Specimens

Figures 7(a) to 7(c) show the reference modeling procedure described earlier and the simplified SWE modeling for the lap-shear specimen with single spot weld. In these models, one end of the specimen is constrained in all directions and the other side of the specimen is subjected to axially symmetrical loading (F_x) and vertically un-symmetrical loading (F_z), respectively, as shown in Figure 7(a). All the analyses carried out using ABAQUS for which the linear shell element based SWE formulation described in Section 2 has been coded as a user element interface referred to as "UEL" in ABAQUS. Outside the spot weld regions (shaded by red color), "S4" linear shell elements in ABAQUS are used to represent the rest of the test specimen geometry. Three element sizes (9.5 mm, 11.875 mm, and 14.25 mm) are used for examining the mesh-sensitivity in structural stress calculation. In addition, the arbitrary shape of SWEs is also used with approximate element size of 9.5 mm to further validate the accuracy and robustness of the developed SWE as shown in Figure 7(c).

It should be mentioned that for the lap-shear specimen with single spot weld, the reference model shown in Figure 7(a) contains 2,596 nodes, 2,457 elements while the simplified model with SWEs shown in Figure 7(b) only contains around 130 nodes and 97 elements.

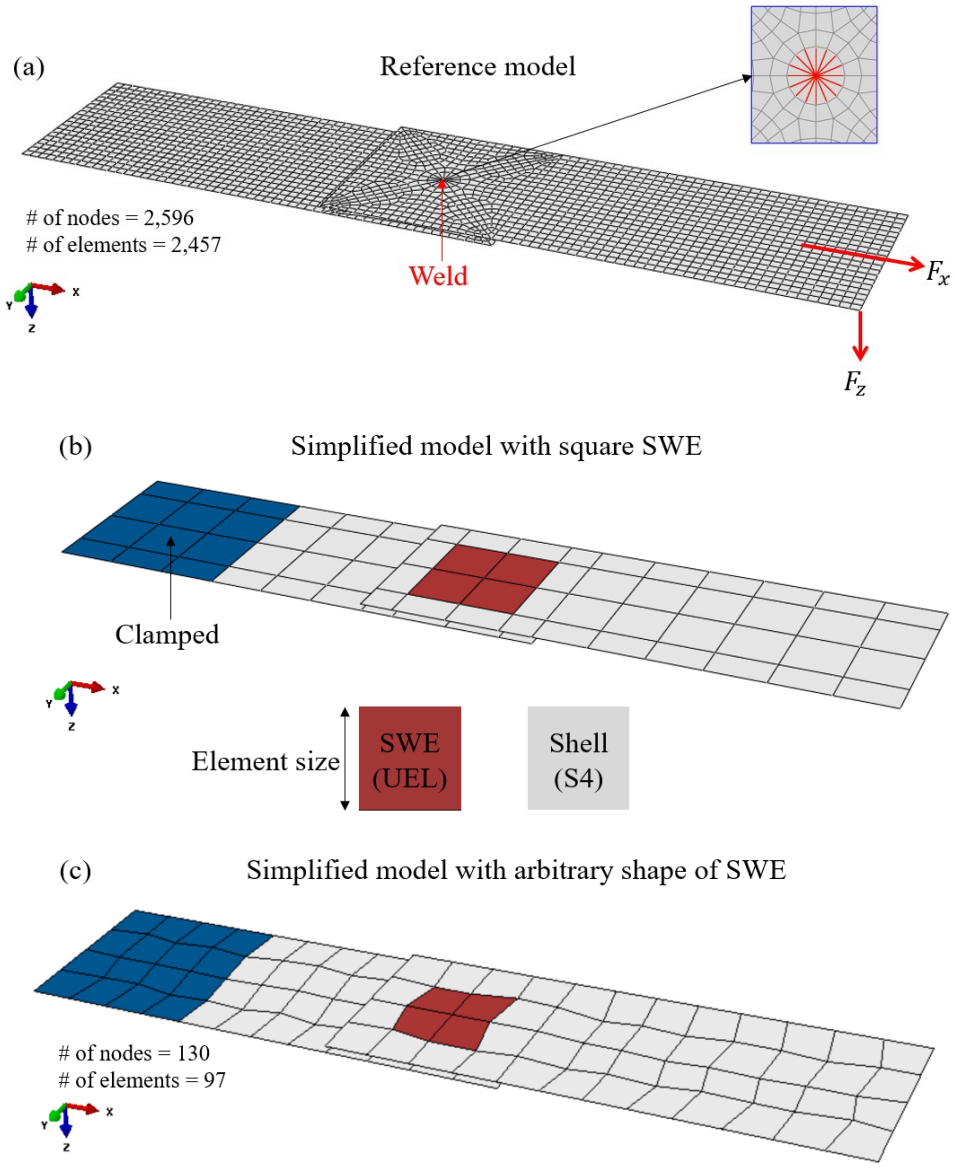

Figure 7. Reference model versus SWE-based shell element model of a lap-shear test specimen: (a) the reference model, (b) simplified model with square SWEs and (c) simplified model with arbitrary shape of SWEs for a lap-shear specimen with single spot weld.

Figure 8 shows the computational results of structural stresses for the lap-shear specimen with single spot weld under the loading along X direction. As shown in Figure 8, the coarse SWE-based model offers the same accuracy as the reference model which entails a significant mesh refinement. All three traction structural stress components computed by using the SWE-

based models share rather similar accuracy, as compared with the results obtained by using the reference model. These are normal, in-plane shear, and transverse shear structural stresses, as shown in Figures 8(a), 8(c), and 8(d), respectively. In contrast, the hybrid structural stress method described earlier [12] can only compute the normal structural stress due to the lack of the corresponding analytical solutions for relevant loading cases [13, 14]. It is worth noting that the hybrid method in Zhang et al. [12] is capable of providing reasonably accurate normal structural stress distribution with slightly lower peak value, as shown in Figure 8(b).

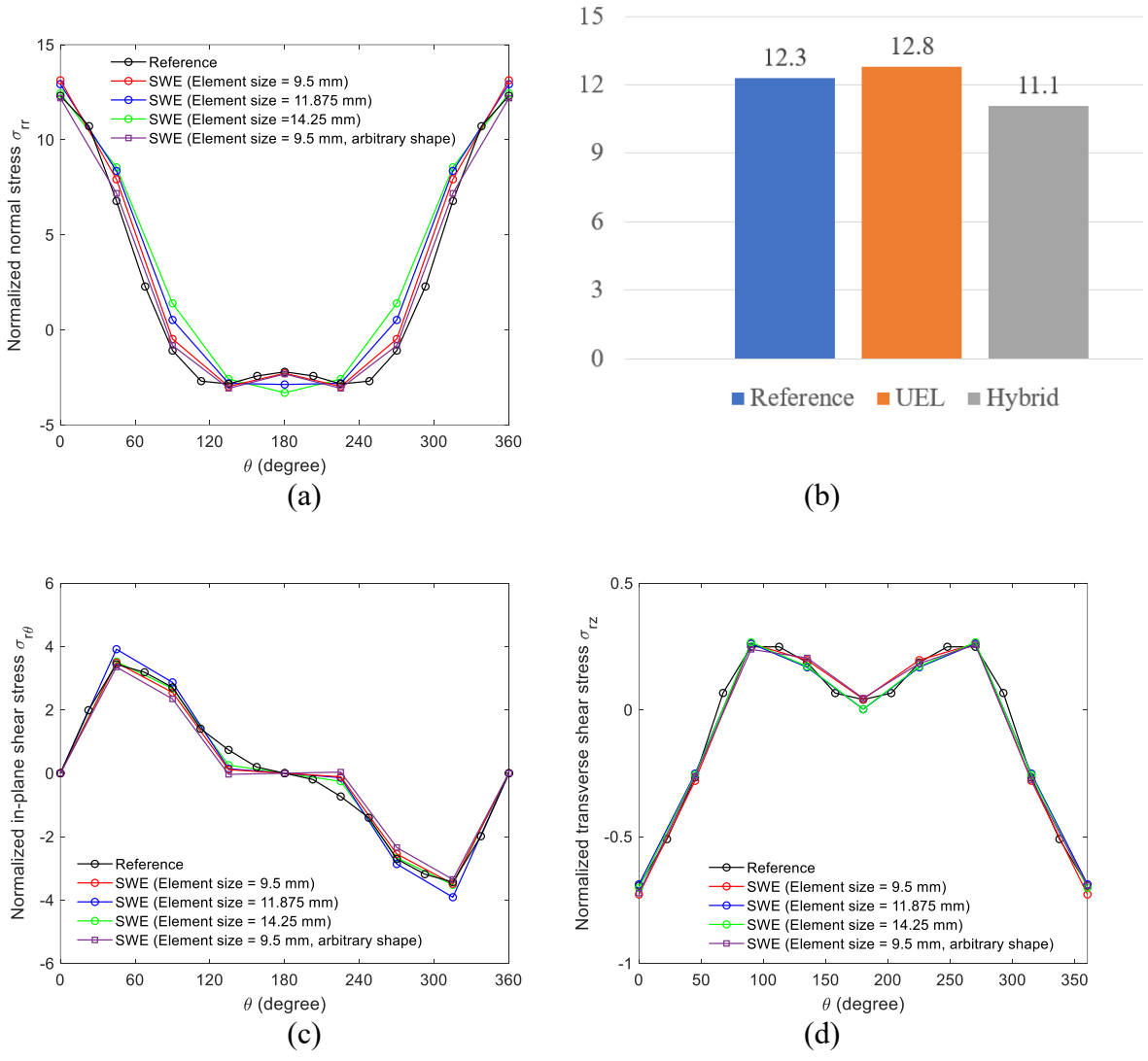

Figure 8. Comparison of all structural stresses along weld nugget edge in a lap-shear specimen loaded axially: (a) normal stress σ_{rr} distribution; (b) the comparison of the maximum normal

stresses σ_{rr}'s from different models; (c) in-plane shear stress $\sigma_{r\theta}$ distribution; (d) transverse shear σ_{rz} distribution.

Similarly, Figure 9 shows the computational normal stress distribution near the weld in the lap-shear specimen under a point force in Z direction. As shown in Figure 9, the simplified model with SWE has more accurate results than those obtained using hybrid method [12]. It should be noted that the relatively inaccurate results from the hybrid method [12] is because the analytical solutions for this unsymmetric point loading is not well-developed as discussed in Zhang et al. [12]. The results shown in Figure 9 also indicates that the simplified model with SWEs have more accurate stress distribution near weld due to a more realistic deformation pattern around spot weld is enforced by Equations (2) and (3).

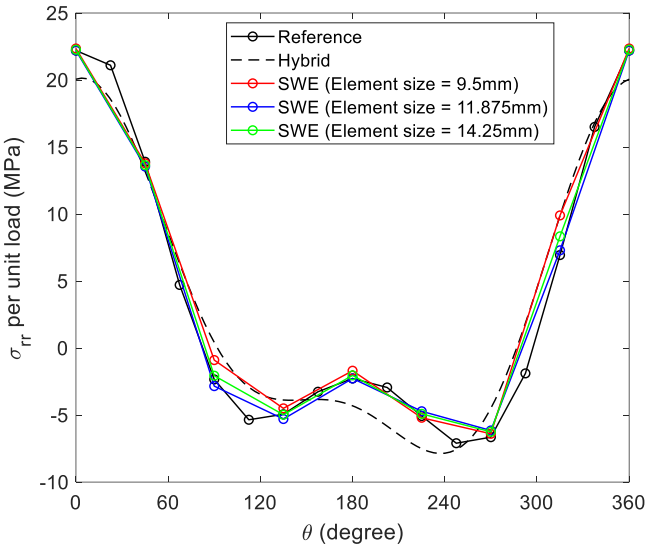

Figure 9. The computational normal stress σ_{rr} distribution near weld in the lap-shear specimen with single spot weld under an unsymmetric vertical point force F_z along Z direction.

3.1.2 Coach-Peel Specimen

Figures 10(a) and 10(b) show the reference FEM and the simplified FEM with SWEs for the coach-peel specimen with single spot weld. Similarly, the SWE is only placed around spot

weld region as shown in Figure 10(b). A symmetric point force F_z is applied at one end of the specimen and the other end is clamped as shown in Figure 10(b). The computational normal stress distribution around spot weld is shown in Figure 11. As shown in Figure 11, the overall normal stress distribution around weld with SWE is in good agreement with that from the reference model. Similarly, the comparison of maximum normal stress using the reference model, the simplified model with SWEs and the hybrid method in Zhang et al. [12] is also provided in Figure 11. It is clearly that the simplified model with SWEs can provide more accurate than the hybrid method [12] with and same modeling simplicity.

It should be mentioned that for the coach-peel specimen with single spot weld, the reference model shown in Figure 10(a) contains 2,738 nodes, 2,593 elements while the simplified model with SWEs shown in Figure 10(b) only contains around 130 nodes and 97 elements.

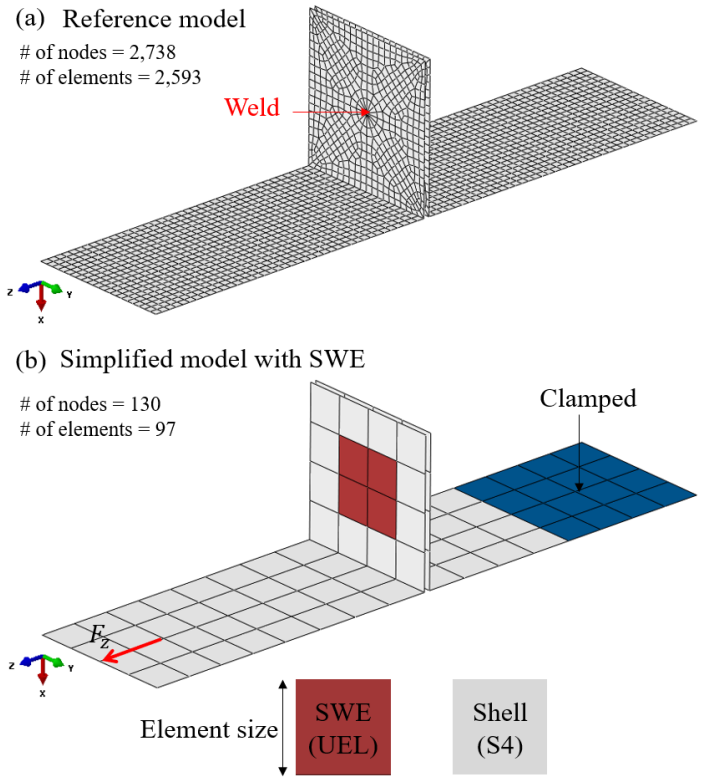

Figure 10. Reference model versus SWE-based shell element model of a coach-peel test specimen: (a) the reference model and (b) simplified model with SWEs for a coach-peel specimen with single spot weld.

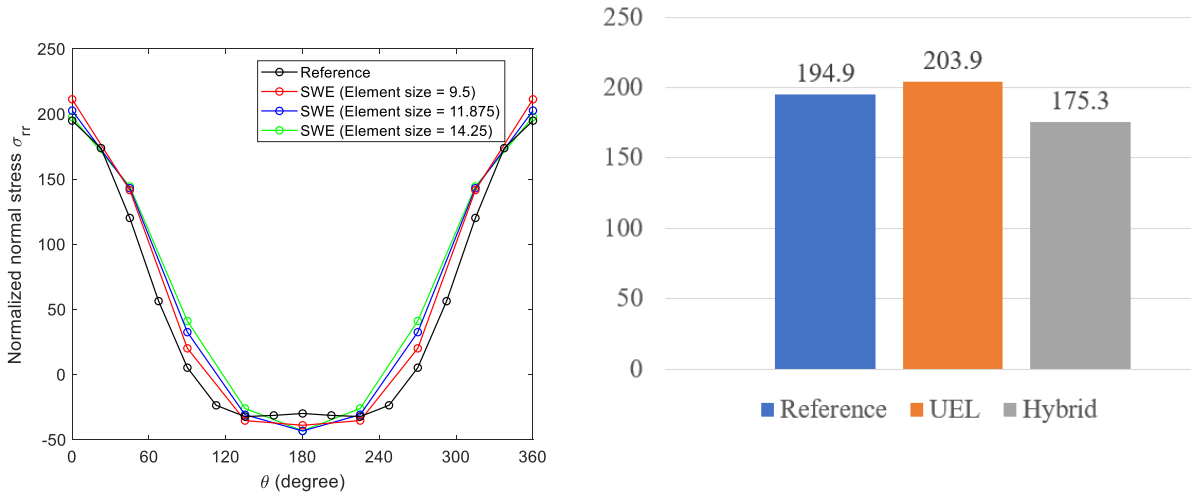

(a) (b)

Figure 11. The computational normal structural stress σ_{rr} near a weld in a coach-peel specimen under a point vertical force along Z direction: (a) normal stress σ_{rr} distribution; (b) the comparison of the maximum normal stresses σ_{rr}'s from different models.

3.2 Multiple Spot-Welded Components

Figure 12 shows the comparison of two-spot weld lap shear specimens modeled using the reference modeling and SWE-based modeling procedures, respectively. The boundary conditions of the lap-shear specimens with double spot welds in series are similar to those for the lap-shear specimen with single weld described in the previous section. The computed normal stress distributions around the 1st and 2nd welds are shown in Figures 13(a) and 13(b), respectively. As shown in Figure 13, the overall normal stress distributions computed with the coarse SWE-based model are as accurate as those with the reference model. Other two traction structural stress results share the similar trend, not presented here due to space limitation.

It should be mentioned that for the lap-shear specimen with double spot welds in series, the reference model shown in Figure 12(a) contains 3,596 nodes, 3,434 elements while the simplified model shown in Figure 12(b) with SWEs only contains around 170 nodes and 130 elements.

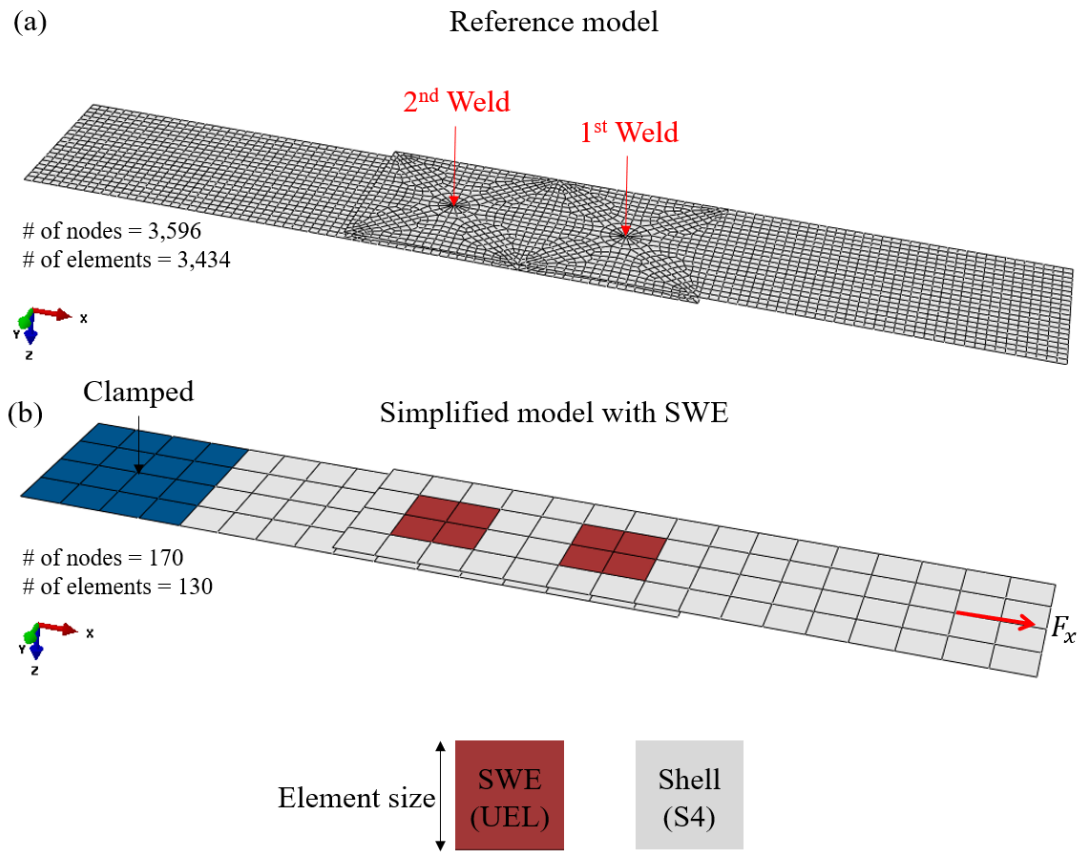

Figure 12. Reference model versus SWE-based shell element model of a lap-shear specimen with double spot welds under a symmetric point force along X direction: (a) the reference model and (b) simplified model with SWEs for a lap-shear specimen with double spot welds.

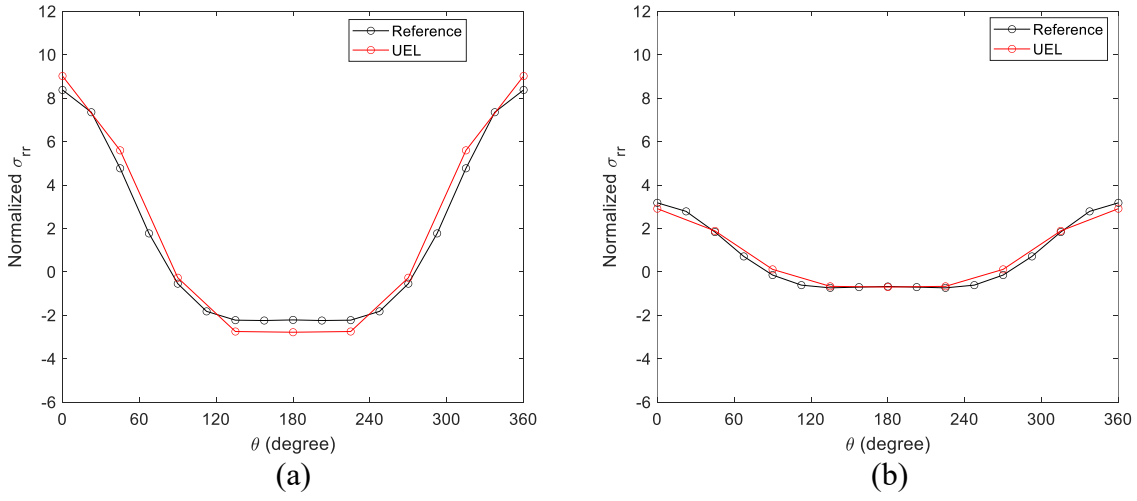

Figure 13. The computational normal stress σ_{rr} distributions in a lap-shear specimen with double spot welds under a symmetric point force along X direction: (a) 1st weld and (b) 2nd weld.

Figure 14 shows the schematics of the modified H-Peel component [10] on which fatigue test data are available. Note that the modified H-Shear component [10] is already shown in Figure 2. Due to symmetry, only one half of the component model is considered here, as shown in Figures 15 and 16 for the modified H-shear and H-peel components, respectively. It is obvious that SWEs offers significant simplicity in model generation in addition to computational resource, comparing the reference modeling procedure.

It should be mentioned that for the modified H-shear specimen, the reference model shown in Figure 15(a) exclude the boundary regions contains 5,628 nodes, 5,325 elements while the simplified model with SWEs shown in Figure 15(b) exclude the boundary regions only contains around 448 nodes and 381 elements. Similarly, for the modified H-peel specimen, the reference model shown in Figure 16(a) exclude the boundary regions contains 4,038 nodes, 3,754 elements while the simplified model with SWEs shown in Figure 16(b) exclude the boundary regions only contains around 336 nodes and 273 elements.

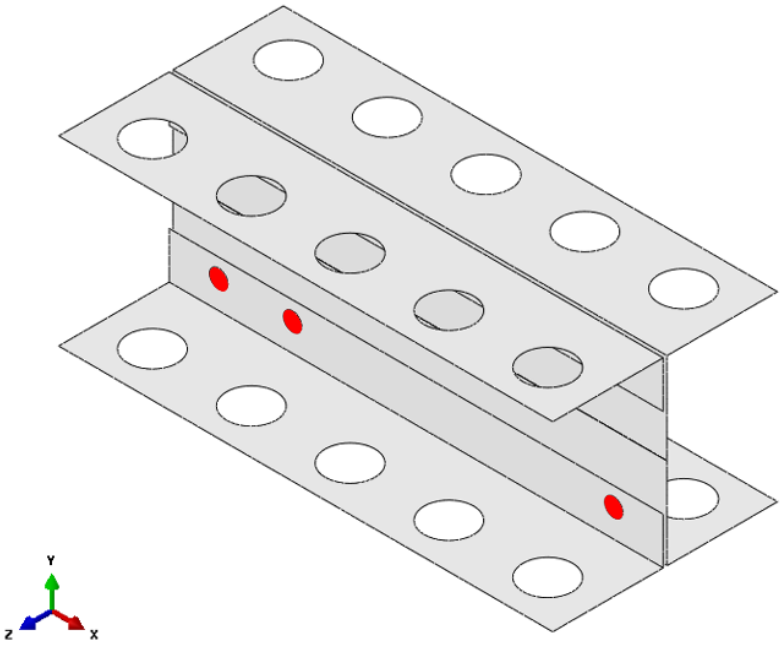

Figure 14. The schematic of the modified H-Peel component[10].

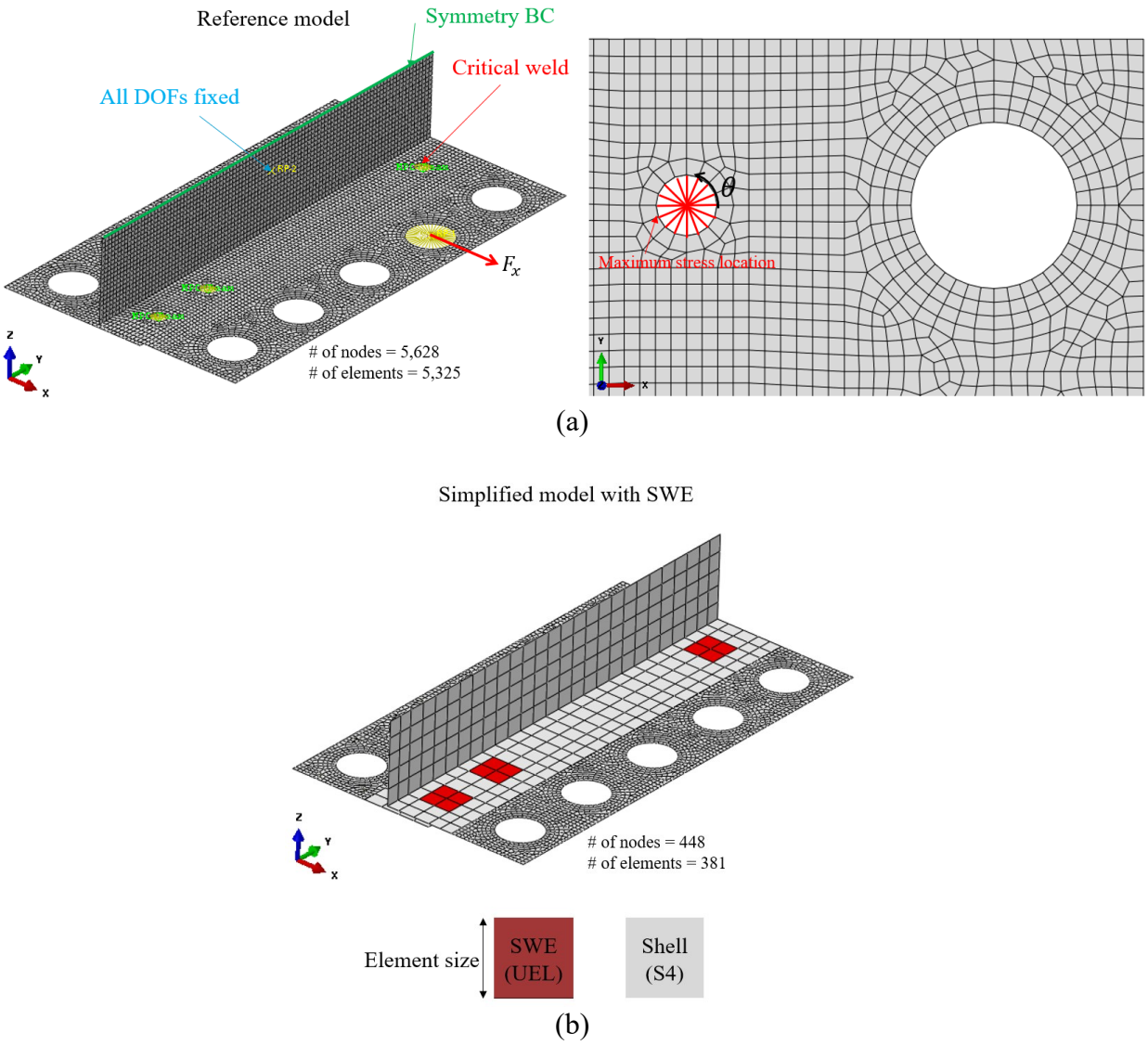

Figure 15. Reference model versus SWE-based shell element model of a modified H-shear components: (a) the reference model with a close-up view around the critical weld and (b) simplified model with SWEs.

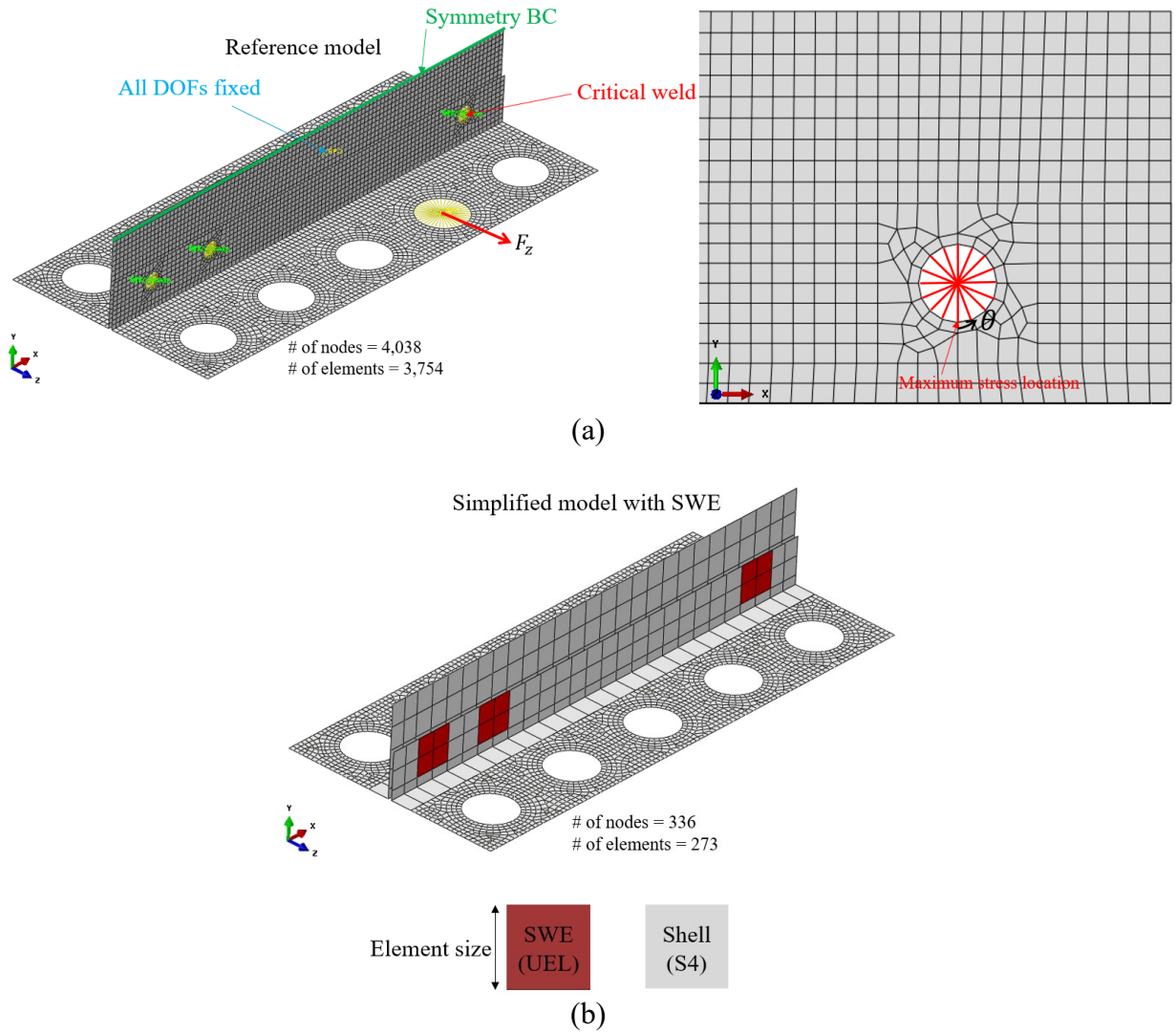

Figure 16. Reference model versus SWE-based shell element model of a modified H-peel components: (a) the reference model with a close-up view around the critical weld and (b) simplified model with SWEs.

For the modified H-shear and H-peel components, the hybrid method in Zhang et al. [12] failed to calculate accurate stress distribution around the critical weld. The reason is because the incorrect deformation pattern around weld if no kinematic constraints are enforced as that in the simplified model with SWEs. The computational results for the modified H-shear and H-peel components are shown in Figures 17(a) and 17(b), respectively. It is clear that the computational

results from the simplified models with SWEs can predict not only the maximum structure stress but also the overall structural stress distribution around welds.

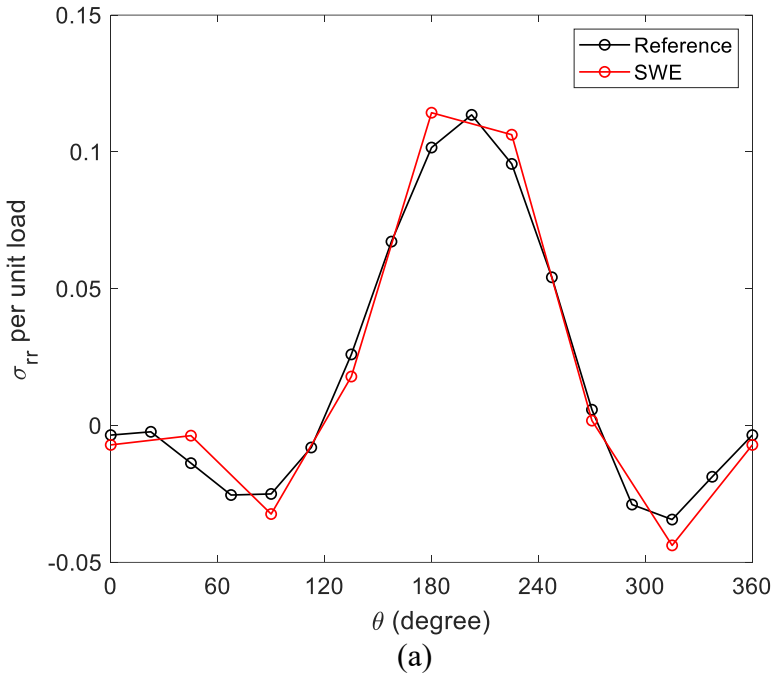

(a)

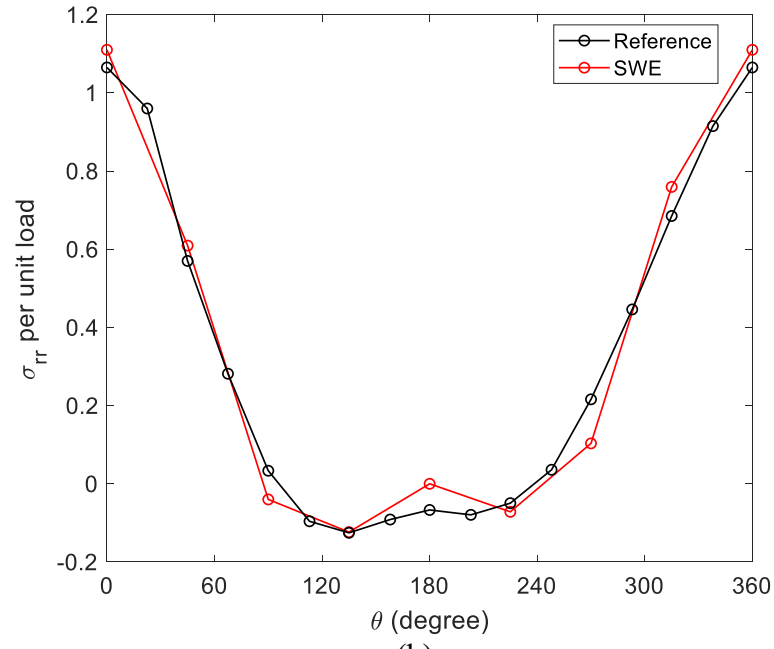

(b)

Figure 17. The computational structural stress σ_{rr} distribution per unit load near critical weld: (a) modified H-shear component; (b) modified H-peel component.

4. Structural Stress Based Fatigue Evaluation for Comp~~Data Correlatilex on – H Type~~ Components

As additional validations of the SWE method, actual fatigue test data (under constant amplitude loading conditions) from the two complex components analyzed in the previous section (Fig. 17) are shown in Fig. 18a ~~The experimental data~~ in terms of applied load range vs cycles to failure. It can be clearly seen that the test data from the two components forms two distinct scatter bands in Fig. 18a. With the peak structural stress values per unit load now available from Fig. 17, ~~for the modified H-shear and H-peel components were shown in Figure 18(a). As expected, the test data presented in terms of the applied load range vs cycles to failure from two types of components are far apart from one another.~~

~~For each load range from the experimental tests shown in Figure 18(a),~~ the corresponding structural stress range $\Delta\sigma_s$ can be simply calculated or scale up by:

$$\Delta\sigma_s = \Delta F \times \sigma_s \tag{15}$$

where ΔF is the experimental load range and σ_s is structural stress per unit load shown in Figure 17. The structural stress range can then be inserted into an equivalent structural stress range parameter

~~It should be emphasized again that for the computational structural stress results in Figure 17, the nodal forces/moments are output at virtual nodes in SWEs positioned at the spot weld periphery for both H-shear and H-peel components as described in Section 2.5. Then, an equivalent structural stress parameter can be defined as follows which has been shown effective for fatigue evaluation of welded components~~ [24] for the correlation of the fatigue test data shown in Fig. 18a, i.e., ~~:~~

$$\Delta S_s = \frac{\Delta\sigma_s}{t^{\frac{2-m}{2m}} \cdot I(r)^{\frac{1}{m}}} \tag{16}$$

where the thickness term $t^{(2-m)/2m}$ with m =3 [24] becomes unity for $t = 1$ (unit thickness) and therefore, the thickness t can be interpreted as a ratio of actual thickness t to a unit thickness, rendering the term dimensionless. With this interpretation, the equivalent ΔS_s retains a stress unit. In addition, $I(r)$ is a dimensionless integral through numerical integration and expressed as a polynomial function of bending ratio r as:

$$I(r)^{\frac{1}{m}} = 0.0011r^6 + 0.0767r^5 - 0.0988r^4 + 0.0946r^3 + 0.0221r^2 + 0.014r + 1.2223 \tag{17}$$

In which r defined as:

$$r = \frac{\sigma_b}{\sigma_b + \sigma_m} \tag{18}$$

The final results according to Eq. (18) are shown in Fig. 18b. The effectiveness of the SWE based method is obvious by comparing Fig. 18a in addition to its simplicity in FE model generation and ability for accommodating coarse FE models. ~~By using the structural stress range calculated at the peak location (Figure 17), the same test data shown in Figure 18(a) can now be presented as an equivalent structural stress range versus cycles to failure, as shown in Figure 18(b). The good fatigue test data correlation shown in Figure 18(b) clearly demonstrate not only the accuracy of the SWE-based structural stress modeling procedure and the effectiveness of the structural stress based parameter for fatigue evaluation of complex welded components, in addition its obvious advantage in simplicity.~~

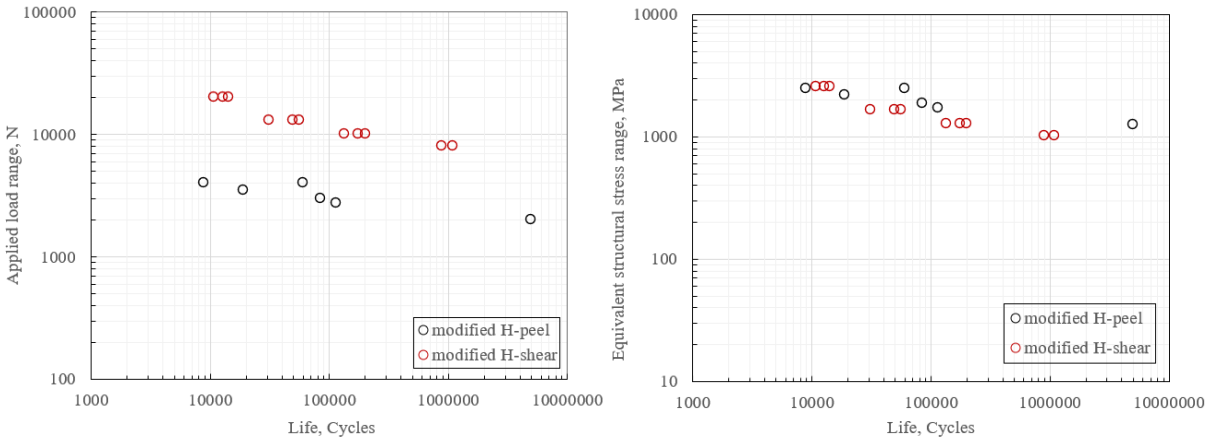

(a) (b)

Figure 18: Correlation of fatigue test data of H-Shear and H-Peel components: (a) Applied load range versus cycles to failure; (b) Equivalent structural stress range versus cycles to failure.

5. Conclusions

In this paper, a special shell element formulation was presented for significantly simplifying the finite element mesh generation effort for representing spot joints in complex structures. Its implementation as a spot weld element (SWE) in the form of a "user element" for working with commercial finite element code (i.e., ABAQUS) was provided for computing the traction structural stresses required for fatigue life evaluation of welded structures. Both single spot-welded lab test specimens and multiple spot-welded components were evaluated using SWE in this paper. In contrast to conventional spot joint modeling procedures, SWE offers the following main advantages:

(1) Significantly simplified efforts in representing spot joint geometry and related kinematic constraints in a finite element model, particularly when dealing with large and complex spot-welded structures.

(2) Drastically reduced number of elements needed for correctly capturing stress concentration behaviors around spot welds.

(3) Mesh-insensitive in traction structural stress calculations, which is essential for achieving reliable fatigue evaluation of welded structures.

Compliance with Ethical Standards

The authors declare that they have no conflict of interest.

References

[1] Bhatti QI, Ouisse M, Cogan S. An adaptive optimization procedure for spot-welded structures. Comput Struct 2011;89(17-18):1697–711.

[2] Junqueira DM, Silveira ME, Ancelotti AC. Analysis of spot weld distribution in a weldment—numerical simulation and topology optimization. Int J Adv Manuf Technol 2018;95(9-12):4071–9.

[3] Yan L, Guo Q-T, Yang S, Liao X-W, Qi C. A size optimization procedure for irregularly spaced spot weld design of automotive structures. Thin-Walled Struct 2021;166:108015. https://doi.org/10.1016/j.tws.2021.108015.

[4] Sun, X., Stephens, E.V. and Khaleel, M.A., 2007. Fatigue behaviors of self-piercing rivets joining similar and dissimilar sheet metals. International journal of fatigue, 29(2), pp.370-386.

[5] Vivio, F., 2009. A new theoretical approach for structural modelling of riveted and spot welded multi-spot structures. International Journal of Solids and Structures, 46(22-23), pp.4006-4024.

[6] Kah, P., Suoranta, R. and Martikainen, J., 2011. Joining of sheet metals using different welding processes. Mechanika, pp.158-163.

[7] Dong P. Quantitative weld quality acceptance criteria: an enabler for structural lightweighting and additive manufacturing. Welding J 2020;99(2):39s–51s.

[8] Rupp A, Storzel ¨ K, Grubisic V. Computer aided dimensioning of spot-welded automotive structures. SAE Technical Paper 1995.

[9] Radaj D, Zhang S. Stress intensity factors for spot welds between plates of unequal thickness. Eng Fract Mech 1991;39(2):391–413.

[10] Gao Y, Chucas D, Lewis C, McGregor IJ. Review of CAE fatigue analysis techniques for spot-welded high strength steel automotive structures. SAE Trans 2001,: 738–50.

[11] Peter, C., Rani, M.A., Hashim, H., Yunus, M.A., Machmud, M.N. and Zin, M.M., 2019, August. A comparative study of CWELD and ACM2 element connectors on the dynamic behaviour of a laser spot welded hat-plate structure under initial stress influence. In Journal of Physics: Conference Series (Vol. 1262, No. 1, p. 012004). IOP Publishing.

[12] Zhang, L., Dong, P., Wang, Y. and Mei, J., 2022. A Coarse-Mesh hybrid structural stress method for fatigue evaluation of Spot-Welded structures. International Journal of Fatigue, 164, p.107109.

[13] Lin P-C, Pan J. Closed-form structural stress and stress intensity factor solutions for

spot welds under various types of loading conditions. Int J Solids Struct 2008;45 (14-15):3996–4020.

[14] Lin P-C, Pan J. Closed-form structural stress and stress intensity factor solutions for spot welds in commonly used specimens. Eng Fract Mech 2008;75(18):5187–206.

[15] Sung S-J, Pan J. Accurate analytical structural stress and stress intensity factor solutions for similar and dissimilar spot welds in lap-shear specimens. Eng Fract Mech 2017;182:265–86.

[16] Salvini P, Vivio F, Vullo V. A spot weld finite element for structural modelling. Int J Fatigue 2000;22(8):645–56.

[17] Dong P. A robust structural stress procedure for characterizing fatigue behavior of welded joints. SAE Trans 2001,:89–100.

[18] Dong P, Hong JK, Osage DA, Dewees DJ and Prager M. The master SN curve method an implementation for fatigue evaluation of welded components in the ASME B&PV Code, Section VIII, Division 2 and API 579-1/ASME FFS-1. Welding Research Council Bulletin, (523). 2010.

[19] Dong P, Hong JK. CAE weld durability prediction: a robust single damage parameter approach. SAE Tech Paper 2002.

[20] Kang H, Dong P, Hong J. Fatigue analysis of spot welds using a mesh-insensitive structural stress approach. Int J Fatigue 2007;29(8):1546–53.

[21] Radaj D, Zhang S. Stress intensity factors for spot welds between plates of unequal thickness. Eng Fract Mech 1991;39(2):391–413.

[22] Khennane, A., 2013. Introduction to finite element analysis using MATLAB® and abaqus. CRC Press.

[23] Abaqus version 6.14 User's Manual.

[24] Kyuba, H. and Dong, P., 2005. Equilibrium-equivalent structural stress approach to fatigue analysis of a rectangular hollow section joint. International Journal of Fatigue, 27(1), pp.85-94.

Appendix A. Element Stiffness Matrix of Square SWE

The followings are the part of entries from the stiffness matrix of SWE with a square shape as shown in Figure 5:

$$k_{1,1}=\frac{1.3\times10^{-3}Et\left(v-3\right)\left(7.7a^4-18.5a^3b+a^2b^2+25.6ab^3-16b^4\right)}{\left(1-v^2\right)}$$

$$k_{2,1}=\frac{2.6\times10^{-3}Et\left(-1.4a^4+2.2a^3b+0.8ab^3-2b^4\right)}{1-v}$$

$$k_{2,2}=\frac{1.3\times10^{-3}Et(v-3)\left(2.5a^4+0.2a^2b^2+0.6ab^3-6b^4\right)}{1-v^2}$$

$$k_{3,3}=\frac{-1.1\times10^{-3}Et\left(10.1a^4-18.5a^3b+1.2a^2b^2+26.1ab^3-22b^4\right)}{v+1}$$

$$k_{4,3}=\frac{-1.8\times10^{-4}Et\left(24.4a^5-18.7a^4b-16.2a^3b^2-101.8a^3+58.3a^2b^3+48a^2b-62.9ab^4+48ab^2+48b^3\right)}{v+1}$$

$$k_{4,4}=\frac{3.6\times10^{-5}Et}{v^2-1}\begin{pmatrix}3.3\times10^3ab-522.8ab^3-529.7a^3b+36.9a^5b+4.1\times10^3a^2v-1.2\times10^3a^4v+105.5a^6v\\-1920b^2v-4.1\times10^3a^2+1.2\times10^3a^4-105.5a^6+1920b^2-616.6a^2b^2\\+217.6a^2b^4-143.8a^3b^3+68.5a^4b^2-37.9a^4t^2+84b^4t^2-80.2ab^3t^2+55.5a^3bt^2\\+616.6a^2b^2v-217.6a^2b^4v+143.8a^3b^3v-68.5a^4b^2v+23a^4t^2v-48b^4t^2v-3.3\times10^3abv\\-4.4a^2b^2t^2+522.8ab^3v+529.7a^3bv-36.9a^5bv+2.9a^2b^2t^2v+76.7ab^3t^2v-55.5a^3bt^2v\end{pmatrix}$$

$$k_{5,3}=\frac{-1.8\times10^{-4}Et\left(-49a^5+118.2a^4b-29.6a^3b^2+163.9a^3-130.6a^2b^3-305.5a^2b+98.9ab^4+14.1ab^2+144b^3\right)}{v+1}$$

$$k_{5,4}=\frac{3.6\times10^{-5}Et}{v^2-1}\begin{pmatrix}146.3ab^3-284a^3b+97.6a^5b-222.3a^4v+53.3a^6v+222.3a^4-53.3a^6\\-117.2a^2b^2+184.1a^2b^4-226.3a^3b^3+25.9a^4b^2-8.5a^4t^2-12b^4t^2+5ab^3t^2\\+13.5a^3bt^2+117.2a^2b^2v-184.1a^2b^4v+226.3a^3b^3v-25.9a^4b^2v-8.5a^4t^2v\\-12b^4t^2v-146.3ab^3v+284a^3bv-97.6a^5bv+5ab^3t^2v+13.3a^3bt^2v\end{pmatrix}$$

$$k_{5,5}=\frac{-3.6\times10^{-5}Et}{v^2-1}\begin{pmatrix}3.3\times10^3ab+1.5\times10^3ab^3-3.7\times10^3a^3b+686a^5b+4.1\times10^3a^2v\\-1.9\times10^3a^4v+263.1a^6v-1920b^2v-4.1\times10^3a^2+1.9\times10^3a^4\\-263.1a^6+1920b^2+429.1a^2b^2+430.7a^2b^4-548.7a^3b^3-282.3a^4b^2\\-53.4a^4t^2+114b^4t^2-155.1ab^3t^2+110.9a^3bt^2-429.1a^2b^2v\\-430.7a^2b^4v+548.7a^3b^3v+282.3a^4b^2v+7.5a^4t^2v-18b^4t^2v\\-3.3\times10^3abv-6.6a^2b^2t^2-1.5\times10^3ab^3v+3.7\times10^3a^3bv\\-686a^5bv+0.7a^2b^2t^2v+1.84ab^3t^2v\end{pmatrix}$$

$$k_{7,1}=\frac{1.1\times10^{-4}Et(v-3)\left(32a^4-69.2a^3b+14.2a^2b^2+47.4ab^3-24b^4\right)}{v^2-1}$$

$$k_{7,2}=\frac{-1.1\times10^{-4}Eat\left(7.2a^3-12.0a^2b+0.77ab^2+3.5b^3\right)}{v-1}$$

$$k_{7,7}=\frac{1.1\times10^{-4}Et\left(v-3\right)\left(-25a^4+50a^3b+13a^2b^2-78ab^3+40b^4\right)}{v^2-1}$$

$$k_{8,1}=\frac{-1.1\times10^{-4}Et\left(19a^4-12a^3b+2.8a^2b^2-78ab^3+72b^4\right)}{v-1}$$

$$k_{8,2}=\frac{-1.1\times10^{-4}Eat\left(v-3\right)\left(-4.5a^3+1.3a^2b+0.69ab^2+4.7b^3\right)}{v^2-1}$$

$$k_{8,7}=\frac{1.1\times10^{-4}Et\left(9.6a^4-9.5a^3b+4.1a^2b^2-14ab^3+8b^4\right)}{v-1}$$

$$k_{8,8}=\frac{-1.1\times10^{-4}Et\left(v-3\right)\left(5.2a^4+3.5a^3b+16a^2b^2+5.7ab^3-44b^4\right)}{v^2-1}$$

$$k_{9,3}=\frac{3.6\times10^{-4}Et\left(9.1a^4-18a^3b+3.4a^2b^2+11ab^3-6b^4\right)}{v+1}$$

$$k_{9,4}=\frac{1.8\times10^{-4}Et\left(4.4a^5-2a^4b+1.6a^3b^2-31a^3-5.2a^2b^3+9a^2b-1.4ab^4+4.7ab^2+32b^3\right)}{v+1}$$

$$k_{9,5}=\frac{1.8\times10^{-4}Et\left(-16a^5+34a^4b-6.1a^3b^2+49a^3-24a^2b^3-79a^2b+11ab^4+5.3ab^2+24b^3\right)}{v+1}$$

$$k_{9,9}=\frac{-1.8\times10^{-4}Et\left(15a^4-23a^3b+1.4a^2b^2+42ab^3-42b^4\right)}{v+1}$$

$$k_{10,3}=\frac{7.2\times10^{-4}Eat\left(1.2a^2+0.17ab-1.8b^2\right)}{v+1}$$

$$k_{10,4}=\frac{9\times10^{-6}Et}{v^2-1}\begin{pmatrix}190ab+230ab^3-23a^3b-1.4e+3a^2v+140a^4v+1.9\times10^3b^2v+1.4\times10^3a^2\\-140a^4-1.9\times10^3b^2-41a^4t^2+24b^4t^2-38ab^3t^2+72a^3bt^2+32a^4t^2v\\-24b^4t^2v-190abv-13a^2b^2t^2-230ab^3v+23a^3bv+14a^2b^2t^2v+47ab^3t^2v-69a^3bt^2v\end{pmatrix}$$

$$k_{10,5}=\frac{9\times10^{-6}Et}{v^2-1}\begin{pmatrix}94ab^3+4a^3b-43a^4v+43a^4-140a^2b^2+7.2a^4t^2+3.5ab^3t^2-12a^3bt^2+140a^2b^2v\\+31a^4t^2v+140b^4t^2v+0.77a^2b^2t^2-94ab^3v-4a^3bv+4.9a^2b^2t^2v-160ab^3t^2v-12a^3bt^2v\end{pmatrix}$$

$$k_{10,9}=\frac{7.2\times10^{-4}Et\left(1.8a^3+4.4a^2b+5.4ab^2-14b^3\right)}{v+1}$$

$$k_{10,10}=\frac{9\times10^{-6}Et}{v^2-1}\begin{pmatrix}2.6\times10^3ab-910a^2v+3.8\times10^3b^2v+910a^2-3.8\times10^3b^2+36a^4t^2-130b^4t^2+89ab^3t^2\\-43a^3bt^2-25a^4t^2v+40b^4t^2v-2.6\times10^3abv+19a^2b^2t^2+13a^2b^2t^2v-78ab^3t^2v+50a^3bt^2v\end{pmatrix}$$

$$k_{11,3}=\frac{-7.2\times10^{-4}\,Et\left(7.7a^3+2.5a^2b-34ab^2+24b^3\right)}{v+1}$$

$$k_{11,4}=\frac{-9\times10^{-6}\,Et}{v^2-1}\begin{pmatrix}80a^4v-90a^3b-340ab^3-80a^4+500a^2b^2-19a^4t^2-72b^4t^2+78ab^3t^2+12a^3bt^2-500a^2b^2v\\+4.8a^4t^2v+72b^4t^2v-2.8a^2b^2t^2+340ab^3v+90a^3bv+1.3a^2b^2t^2v-85ab^3t^2v+12a^3bt^2v\end{pmatrix}$$

Appendix B. Formulation and Validation of Arbitrary Shape of Special Weld Element (SWE)

The formulation of special weld element (SWE) is based on two linear four-nodes Mindlin shell element with consideration of weld region constraints. The formulation of a linear four-nodes Mindlin shell element can be found in many textbooks [22] and will not be elaborated here. Instead, this Appendix will assume the stiffness matrix of the two linear four-nodes Mindlin shell elements are available and focus on providing the equations and procedures to enforce the force/moment equilibrium equations as explained in Section 2.2 as well as the stiffness matrix assembly procedures of SWE.

With the kinematic constraints in Equation (2) and the force and moment equilibrium conditions in Equation (3), the SWE with nodes 1, 2, 3 and 4 can be assembled based on the element stiffnesses of Element #1 and Element #2. The calculation procedures are shown in Figure B1 and summarized as below:

(I) A unit displacement vector U containing displacement field at nodes 1, 2, 3, and 4 is generated. This unit displacement vector contains only one nonzero entry in a 24 by 1 displacement vector.

(II) The kinematic constraints, Equation (2), is applied to generate the displacement values at virtual nodes v1, v2, v3. The displacement values at nodes 2, 3, and 4 are preserved. By using Equation (2), two displacement vectors U^1 for Element #1 (nodes v1, 2, 3, v2) and U^2 for Element #2 (v2-3-4-v3) can be calculated.

(III) With the element stiffness matrices K^1 of Element #1 and K^2 of Element #2, the nodal forces at nodes v1, v2, v3, 2, 3, and 4 can be calculated as

$$\begin{aligned} K^1U^1 &= F^1 \\ K^2U^2 &= F^2 \end{aligned} \tag{B1}$$

where F^1 and F^2 are the force vectors for Element #1 and Element #2, respectively .

(IV) The force and moment equilibrium conditions, Equation (3), is then applied to transfer the nodal forces at virtual nodes v1, v2, and v3 to those at node 1. Then the force vector F for the SWE with nodes 1, 2, 3, and 4 resulted from the unit displacement vector U in (I) can be calculated, which is the corresponding column of the SWE stiffness matrix.

(V) Finally, repeat the steps (I) to (IV) with different nonzero entry for the unit displacement vector U in (I) such that the entire SWE stiffness matrix can be calculated.

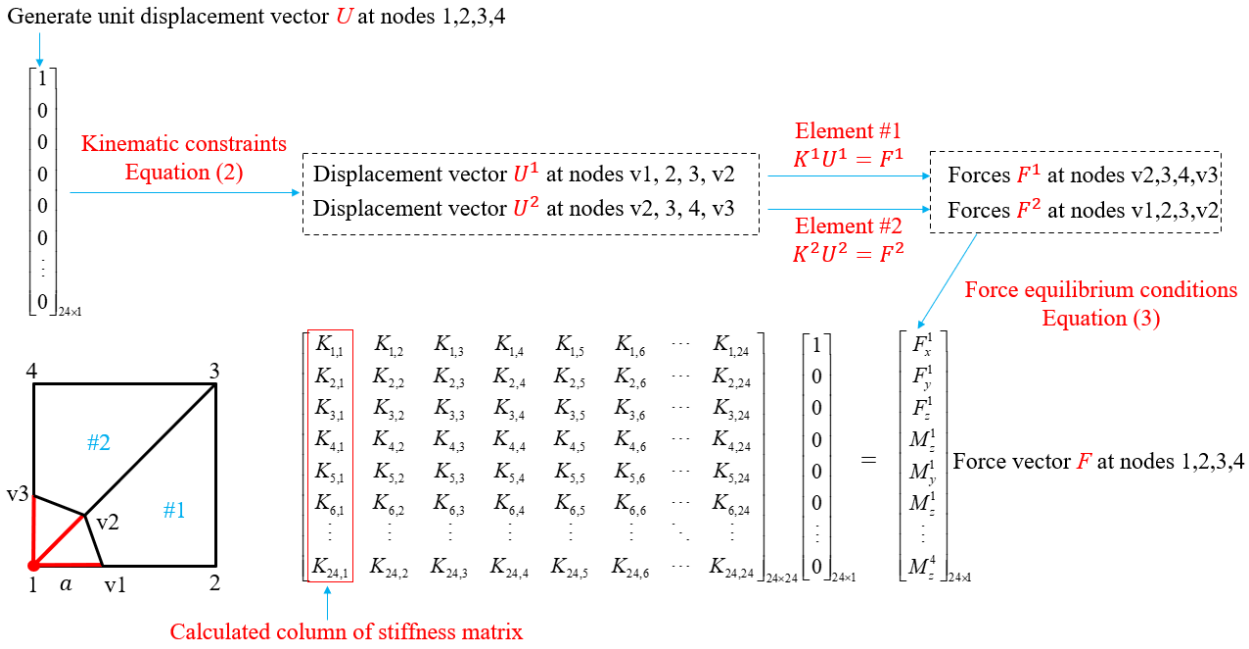

Figure B1. The calculation process of the stiffness matrix of SWE.

It should be noted that the expression of the close-form stiffness matrix is usually difficult to be obtained for irregular shape of the SWE with the nodes 1, 2, 3, and 4, the numerical integration procedure is needed which is similar to any finite element formulation in commercial finite element solvers.

The validation of the SWE is tested using one quarter of weld region as shown in Figure B1. In Figure B2, the specified boundary conditions are placed at the nodes 1, 2, 3 and 4. The

input file (.inp file) for Abaqus and the command window to use the SWE are shown in Figure B3. It should be mentioned that the preparation of Abaqus input file for the SWE model is automatically generated using a Python script. The summarized nodal force results from the SWE model are documented in Table B1 and compared with those from the reference model. In Table B1, the errors between the SWE model and the reference model are also provided, for example, (1.2%) represents the absolute error is 1.2%. The results indicate that the developed SWE has similar accuracy compared with Abaqus shell element S4.

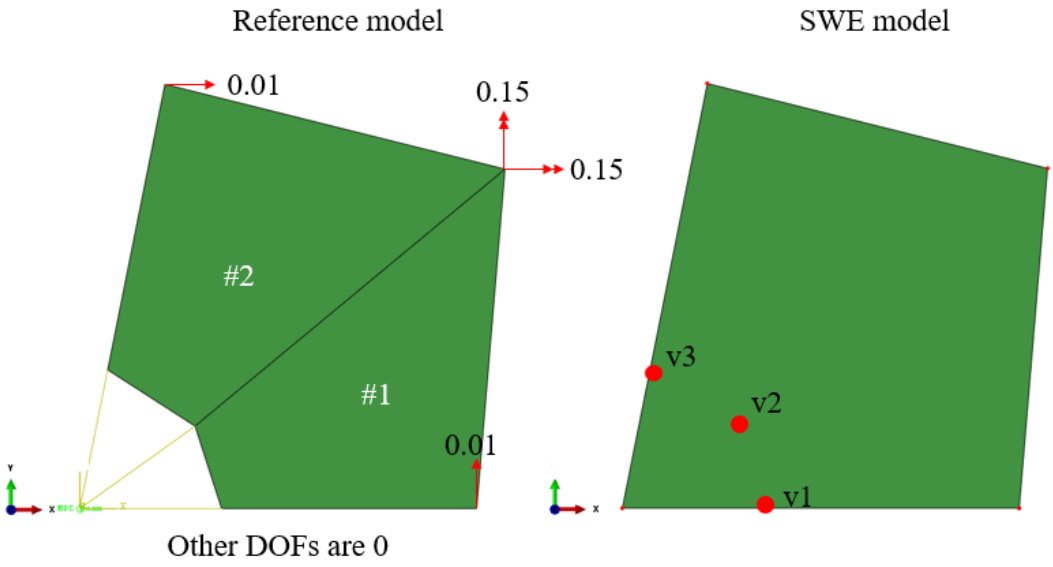

Figure B2. One element test using SWE for modeling of one quarter of weld region.

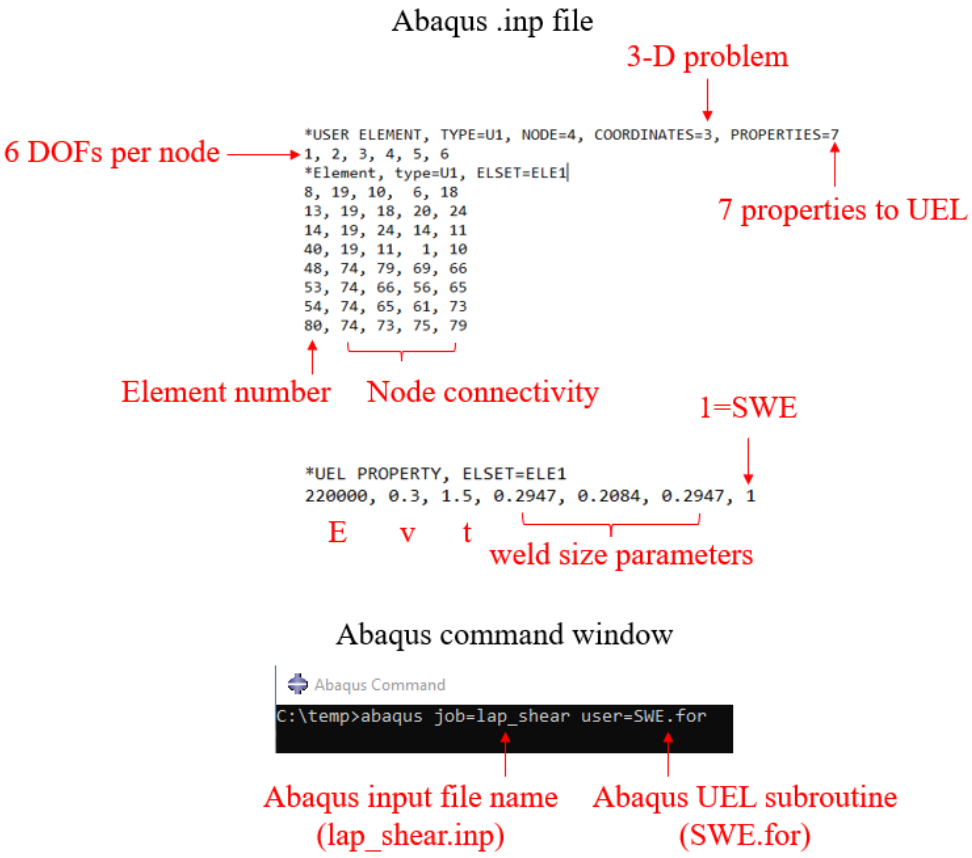

Figure B3. An example of Abaqus input file and command window to use the SWE.

Table B1. The output nodal forces/moments at virtual nodes from one element test.

	Reference Model			Single SWE		
	v1	v2	v3	v1	v2	v3
NFORC1	2380	1198	-4265	2354 (1.0%)	1181 (1.3%)	-4237 (0.6%)
NFORC2	-5667	6930	3403	-5820 (2.7%)	6741 (2.7%)	3435 (0.9%)
NFORC3	-7644	-4316	16046	-7431 (2.7%)	-4212 (2.4%)	15729 (2.0%)
NFORC4	480836	-1132840	49261	479070 (0.4%)	-115480 (2.0%)	49870 (1.2%)
NFORC5	-57211	-847190	816958	-56804 (0.7%)	-857091 (1.2%)	794010 (2.8%)